Check for updates

A changeable critical state for a switchable photocurrent direction *via* the photo-electrochemical photocurrent polarity switching effect in BiFeO₃ nanoparticulate films†

Ajay, Jyoti Saroha and Pravin Popinand Ingole 📖 *

The photoelectrochemical photocurrent switching (PEPS) effect to change the photocurrent direction from cathodic to anodic *via* external bias is an important phenomenon. Specifically, tuning the critical state or the potential corresponding to a switchable photocurrent direction through easily controllable parameters is crucial for developing efficient photo-electrocatalyst systems. Although the PEPS effect has been reported in quite a few recently published studies, the changeable critical state has not yet been demonstrated. In this study, for the first time, we present a photoelectrochemical (PEC) system based on bismuth ferrite (BiFeO₃) nanoparticulate films that demonstrates a changeable critical state controlled *via* the composition of an electrolyte medium. In particular, the ionic strength (tuned *via* addition of inert salt) and the concentration of dissolved oxygen in an electrolyte medium are noted to dictate the potential corresponding to the critical state. Importantly, we demonstrate that this potential can be predicted using the Nernst equation by considering electrolyte energy level rearrangement and the kinetic theory of semiconductor electrodes. This study enhances the understanding of carrier transport in PEC activities and enables precise control over the reversal of the photocurrent direction that may pave the way for developing sophisticated multifunctional photoelectric devices and efficient photo-electrocatalyst systems.

1 Introduction

Photoelectrochemical (PEC) systems with bipolar photocurrent, *i.e.*, with both the cathodic and anodic polarity, are important for a variety of applications including the sensing technology and water splitting.[1–4] The ability to manipulate the photocurrent direction in bipolar PEC systems, *via* the photo-electrochemical photocurrent switching (PEPS) effect, represents a significant advancement across technologies.[5–8] The emergence of this effect in semiconductor materials is contingent upon specific electronic band structures compared to the dynamic Fermi levels of electrolytes that delineate the conditions for change in PEC reactions at the semiconductor/electrolyte interface. The degree and type of PEC reaction can be significantly influenced by varying both the composition of electrolytes and the surface electronic properties of semiconductors as per the theory of semiconductor electrode dynamics.[5] To realize practical PEC switching devices, semiconductor electrode materials with appropriate band edge

positions, narrow band gaps for visible light absorption, and ease of fabrication using earth-abundant materials are highly desirable. The presence of electrolytes in PEC systems offers additional and distinct advantages, encompassing both physical processes, such as excitation, diffusion, and carrier drift reminiscent of those found in solid-state transistors in semiconductors, and chemical processes, such as interfacial ion diffusion, migration, redox reactions, and PEC reactions that are absent in solid-state transistors.[9]

Currently, the prevailing strategies for switching the photocurrent polarity involve changing either the excitation wavelength or the bias voltage or intensity of incident light, among which the use of external bias is more convenient and advantageous.[4,10–13] Predominantly, these methods are targeted towards tailoring the surface electronic properties of semiconductor nanostructures and modulating the electronic effects in molecular hybrids.[8,14–17] This is because conventional semiconductor materials, such as $BiVO_4$, $SrTiO_3$,[18] Fe_2O_3, *etc.* typically display unidirectional photocurrent behaviour due to their electrochemical diode-like properties.[19–21] Recently, switchable photocurrent behavior has been reported in TiO_2 nanosheets layered with polyaniline,[22] as well as in thin film electrodes comprising a blend of n-type *N*-doped TiO_2 and p-type CuI[12] and in CuPc/β-Ga_2O_3 p–n junctions,[23] demonstrating diverse

Department of Chemistry, Indian Institute of Technology Delhi, Hauz Khas, New Delhi, India-110016. E-mail: ppingole@chemistry.iitd.ac.in; Fax: +91 11 2658 1102; Tel: +91 11 2659 7547

† Electronic supplementary information (ESI) available. See DOI: https://doi.org/10.1039/d4sc04504a

approaches for achieving photocurrent switching. However, such configurations generally involve multi-material systems, making it unusual for single-phase metal oxide photo-electrodes to exhibit both cathodic and anodic photocurrent polarity. Only a limited number of studies have reported the bipolar photo-response (*i.e.*, PEPS effect) in single-phase metal oxides, such as Fe_2O_3, TiO_2, and $BiFeO_3$. Besides, attributions to extrinsic factors such as the presence of alkaline electrolytes and dissolved oxygen are often lacking.[24–26] Thus, the discovery of single-phase metal oxides capable of intrinsic switchable photocurrents and comprehensive elucidation of the PEPS effect presents intriguing prospects for advanced PEC devices.

Another important aspect of the PEPS effect is that the electrolyte properties also have a significant impact on the photocurrent as well as the polarity reversal. Unfortunately, the influence of electrolyte on PEC detection devices and tuning of electrolyte properties for the PEPS effect has been overlooked in terms of its impact on both the photocurrent polarity and the photocurrent density. Nevertheless, the effect of electrolyte pH on the direction of photocurrent in $MnPS_3$ photodetectors has been recently reported by Geng et al.,[5] where the photocurrent polarity was noted to reverse at an alkaline pH of 11. Below pH $\sim$ 11, the photocurrent is cathodic, while anodic photocurrent is observed above pH 11, marking pH 11 as the critical state. However, variation of the critical state or controlling the potential corresponding to the critical state for the PEPS effect, through easily and externally controllable parameters, is essential for further development of advanced photodetection and PEC devices. In this context, Guo et al. introduced strategies to regulate the switching potential in photoelectrochemical systems by varying the β-Ga_2O_3 shell thickness in α/β-Ga_2O_3 structures,[27] altering $Ti_3C_2T_x$ modification levels on nanorod arrays[28] and controlling crystalline phases in Ga_2O_3.[29] These approaches underscore the significance of structural modifications in tuning photocurrent switching behavior, highlighting the need to further explore external parameters for optimizing the PEPS effect in PEC devices.

In this study, for the first time, we demonstrate a tuneable critical state controlled through the ionic strength of an electrolyte over a wide range of switching potentials from 0.78 to 0.89 V ($\Delta E = 110$ mV). $BiFeO_3$ (BFO) was chosen due to its promising candidature for a range of applications, owing to its room-temperature multiferroic, ferroelectric, and magnetic properties. Due to the unique band structure, suitable Fermi level position, and mid-gap states, it possesses the unique ability to switch the photocurrent polarity under applied bias.[30–33] Recent research has highlighted the potential of BFO as a photocatalyst, leveraging the spontaneous dipole moment to enhance carrier separation and to accelerate chemical reaction rates. Another important consideration behind selecting BFO as an electrode material for studying the PEPS effect is the requirement of an appropriate band structure for redox reactions in electrolytes under illumination.[24]

We hypothesize that altering the composition of electrolyte *via* changing the ionic strength through the addition of an inert electrolyte and the concentration of dissolved oxygen would alter the energy level in an electrolyte without changing its pH.

This adjustment influences solvent-ion interaction and the concentration of oxidized and reduced species at the electrode–electrolyte interface. Consequently, it alters the dynamics of charge carriers before and after equilibrium, as the position of the electrolyte Fermi level significantly impacts the width of the space charge layer of the semiconductor at the interface. The variable critical state in single phase BFO controlled through externally adjustable parameters such as modification of the electrolyte without affecting the pH of the medium presents a unique approach to harness the potential of technologically important BFO-based materials for PEC applications.

2 Results and discussion

In order to observe the PEPS effect in a bipolar metal oxide nanomaterial without p–n junction hybrids, it has been reported that the phase-purity is crucial. Therefore, single-phase BFO was synthesized *via* a modified protocol based on controlled thermal decomposition of a Bi–Fe glycolate single molecular precursor to give precise control over stoichiometry (Scheme S1†).[34,35] The detailed methodology and the relevant details regarding synthesis and material characterization are given in the ESI.† Typically, 20 mL of ethylene glycol (EG) was transferred into a pre-cleaned glass beaker and bismuth nitrate pentahydrate (1 mmol) was added to it at room temperature under continuous stirring. Then, 1 mmol of iron nitrate nonahydrate was dissolved in the above transparent solution under stirring. The resultant solution with a pH of $\sim$5 was heated at 180 °C for 3 h under continuous stirring and the obtained slurry was cooled down to room temperature and then precipitated out using ethanol. The precipitate was centrifuged, washed with ethanol, and dried in an oven at 60 °C overnight to get Bi–Fe glycolate.

The thermogravimetric analysis (TGA) of Bi–Fe glycolate as shown in Fig. S1† was performed to decide the calcination temperature, which displays a characteristic weight loss comprising two distinct steps. An initial weight loss ($\sim$4%) below 100 °C is attributed to the desorption of physisorbed water molecules, while a subsequent weight loss ($\sim$54%) within 100 to 420 °C is ascribed to the decomposition of organic moieties and the release of chemically bonded EG. Notably, no further weight loss beyond 420 °C was noted implying the completion of the decomposition process. Therefore, Bi–Fe glycolate was subjected to air calcination at 500 °C for 3 hours with a heating rate of 2 °C min^{-1} inside a muffle furnace and the obtained sample was named BFO NPs. Finally, the as-synthesized BFO NPs were ground for 30 min and stored for further characterization studies.

The powder X-ray diffraction (pXRD) pattern of BFO depicted in Fig. 1(a) exhibits well-defined and intense diffraction peaks at 2θ of 22.4°, 31.9°, 32.1°, 39.5°, 45.7°, 51.8°, and 45.7° corresponding to the crystallographic planes (101), (012), (110), (021), (202), (113), and (122), respectively, that match with monoclinic $BiFeO_3$ (JCPDS card no. #00-020-0169). The absence of any discernible secondary phases (within the limits of detection) indicates the highly crystalline nature and phase purity of the BFO NPs. The FTIR analysis (Fig. 1(b)) depicts characteristic
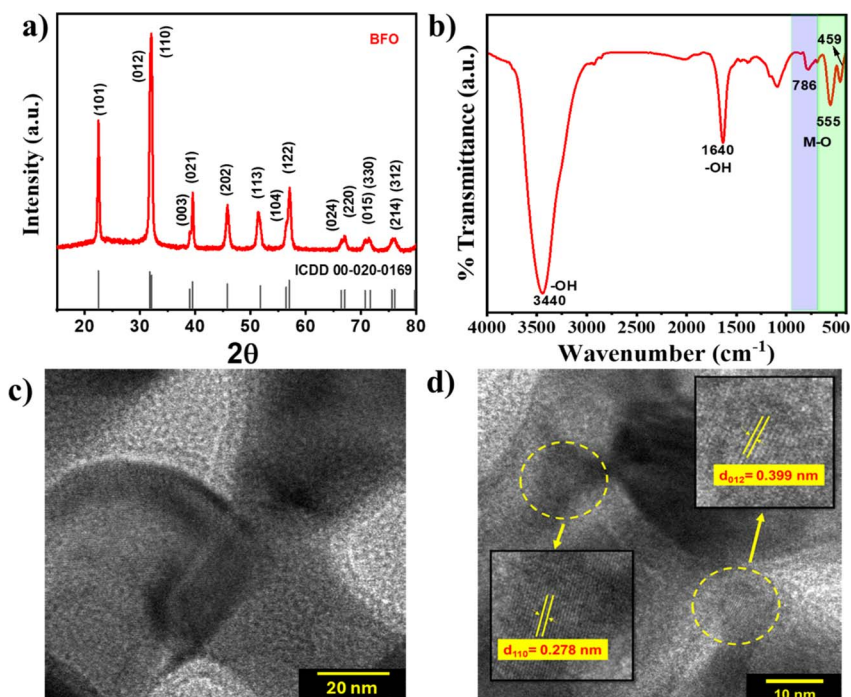
Fig. 1 (a) XRD pattern, (b) FTIR spectrum, and (c & d) HRTEM images with different magnifications of BFO NPs.

absorption bands at around 459 and 555 cm^{-1} ($\nu1$) for Fe–O stretching vibrational mode of octahedral FeO_6 groups supporting the formation of the $BiFeO_3$ phase.[36] The appearance of a distinct Fe–O peak at 786 cm^{-1} ($\nu2$) is infrequent in amorphous materials because of their lack of short-range order, further supporting the formation of phase-pure $BiFeO_3$ as required for the PEPS effect.[37]

High resolution transmission electron microscopy (HR-TEM) images of BFO NPs are shown in Fig. 1(c) and (d) that depict lattice fringes with an interplanar spacing of 0.278 and 0.399 nm corresponding to lattice planes (110) and (012), respectively. Low-resolution TEM and field-emission scanning electron microscopy images depicted in Fig. S2(a) and (c),† respectively, show nanoparticles of elongated spherical symmetry with an average length of 47 ± 5 nm [Fig. S2(b)†]. The diffraction rings corresponding to various lattice planes are evident from the selected area electron diffraction (SAED) pattern shown in Fig. S2(d),† which also corroborates the findings from XRD analysis indicating the polycrystalline nature of BFO NPs.

X-ray photoelectron spectroscopy (XPS) was performed to identify the elemental composition and energy states within the BFO NPs. The XPS survey spectra provided in Fig. S3† revealed the presence of Bi, Fe, O, and C elements. Carbon was detected as a common impurity resulting from sample handling and exposure to air during preparation. The Bi 4f core level (CL) spectrum shown in Fig. 2(a) is deconvoluted into a Bi $4f_{7/2}$ peak at 158.5 eV and Bi $4f_{7/2}$ peak at 163.0 eV, indicating the presence of Bi^{3+}.[38,39] Notably, no features related to metallic Bi and/or Bi_2O_3, which typically appear at binding energies of 157.0 and/or 159.3 eV, respectively, were seen. The deconvoluted Fe 2p CL

XPS spectrum displayed in Fig. 2(b) exhibited peaks corresponding to Fe^{2+} (Fe $2p_{3/2}$ ~709.4 eV and Fe $2p_{1/2}$ ~721.5 eV) and Fe^{3+} (Fe $2p_{3/2}$ ~711.4 eV and Fe $2p_{1/2}$ ~724.5 eV) and satellite peaks at ~718.5 eV and 732.6 eV.[39] The O 1s CL spectra [Fig. 2(c)] were deconvoluted into three peaks: a peak at 529.5 eV represents lattice oxygen from BFO (O_L) and a peak at 531.0 eV was attributed to oxygen adjacent to an oxygen vacancy (O_v) (also referred to as dangling oxygen bonds). The peak at the highest binding energy (532.4 eV) indicates adsorbed oxygen species, possibly originating from vacancy healing under ambient conditions.[39] The presence of oxygen vacancies is known to be an important factor in the PEPS effect.

The presence of defect states, particularly those associated with oxygen vacancies within the BFO structure, is also demonstrated using the UV-Vis absorption spectrum of BFO (Fig. 2(d)) that depicts a gradual increase in absorbance starting from 650 nm, followed by a pronounced increase at around 460 nm, due to sub-bandgap transitions.[40] The band gap energy (~1.9 eV) estimated from the Tauc plot (inset, Fig. 2(d)) is governed by the orbital overlap between O 2p and Fe 3d levels. This indicates BFO as a charge-transfer semiconductor.[26] Furthermore, the electronic band structure of BFO (Fig. 2(f)) was established by determining its valence band maxima (VBM) using the XPS valence band spectrum depicted in Fig. 2(e). The VBM of ~−5.77 eV *vs.* vacuum was then subtracted from an optical band gap of 1.9 eV to estimate the conduction band minima (CBM) that was found to be at ~−3.87 eV *vs.* vacuum. The ultraviolet photoelectron spectroscopy (UPS) spectra, as shown in Fig. S4,† revealed a secondary electron cutoff energy of 17.60 eV. Using eqn (1) (ESI†), the work function (Φ) was calculated to be 4.5 eV. The Fermi level (E_f) was determined to
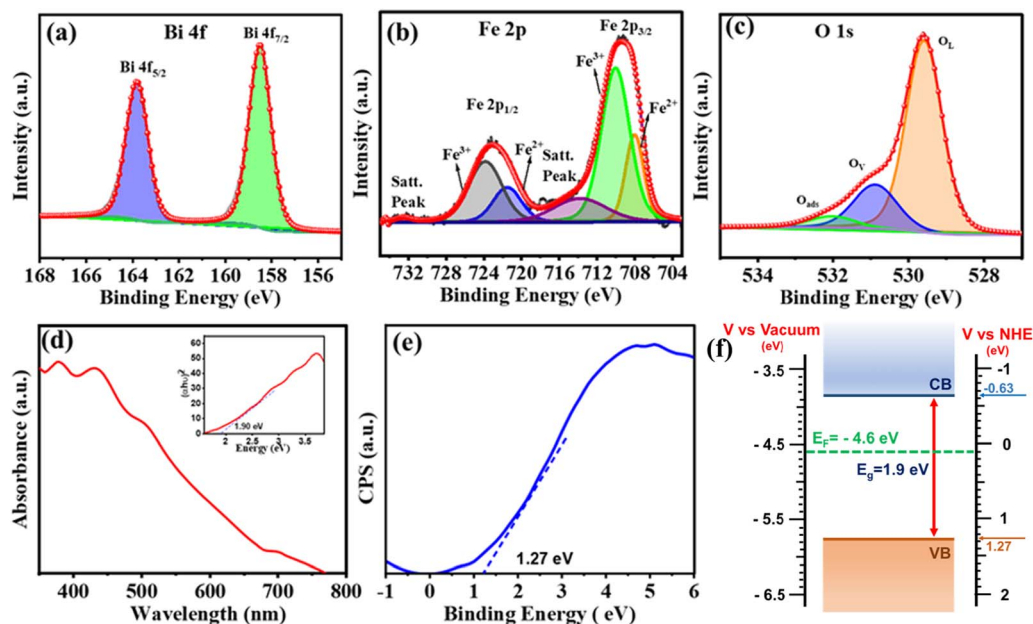
Fig. 2 High-resolution CL XPS spectra for Bi 4f (a), Fe 2p (b), and O 1s (c) elements of BFO NPs. (d) UV-Vis absorption spectrum with the corresponding Tauc plot in the inset, (e) valence band edge position determined using XPS, and (f) band edge alignment with a Fermi level diagram.

be at -4.5 eV, indicating its position between the CBM (-3.87 eV vs. vacuum) and VBM (-5.77 eV vs. vacuum), confirming the mid-gap alignment and providing critical insight into the electronic properties of the material.

2.1 Photoelectrochemical characterization towards the PEPS effect

To verify if the as-synthesized BFO NPs would demonstrate the PEPS effect, a BFO nanoparticulate film was deposited on an FTO quartz substrate and studied for photocurrent generation as a function of applied potential under the intermittent chopping of incidence light. The PEC measurements were performed using a Zahner Zennium Pro 212 equipped with an LED driver (450 nm, 0.65 A) in a standard three electrode single-compartment cell assembly using Ag/AgCl/Cl$^-$ (saturated with KCl) as a reference electrode, a Pt mesh as a counter electrode and BFO nanoparticulate film coated FTO as a working electrode. The working electrode was fabricated by drop casting catalyst ink (10 µL) prepared by mixing 1 mg of BFO NPs with 100 µL isopropanol followed by sonication for *ca.* 30 minutes on an FTO quartz substrate (with dimensions of 1.0 cm × 1.0 cm) and then drying under ambient conditions before using it for PEC measurements. Fig. 3(a) illustrates photocurrent *vs.* applied potential (V_{app}) curves measured for the BFO nanoparticulate film electrode in Na$_2$SO$_4$ under simulated solar (AM 1.5) light illumination with intermittent chopping. A clear switch in the photocurrent direction from cathodic to anodic was noted. An enlarged portion of the plot [Fig. 3(b)] clearly illustrates this switchable photocurrent direction at a switching potential (V_{switch}) of 0.78 V vs. RHE. Fig. 3(c) illustrates the transient photo-response of the material at V_{switch}, *i.e.*, at 0.78 V

vs. RHE, and the potentials slightly above and below V_{switch} that clearly represent the differences in the dynamics of photo-generated charge carriers inside the space charge region of the BFO semiconductor. At $V_{app} > V_{switch}$ (at 0.85 V vs. RHE), the photocurrent direction is anodic, while it is cathodic at $V_{app} < V_{switch}$ (at 0.75 V vs. RHE). At $V_{app} = V_{switch}$ (0.78 V vs. RHE), a unique critical or confusing state exists: when light is switched to ON, the photocurrent first increases and then decreases, whereas when the light is switched to OFF, the photocurrent first decreases and then increases. In other words, below 0.78 V RHE, the behaviour of BFO resembles that of a p-type photocathode with the predominance of cathodic photocurrent, while beyond 0.78 V RHE, the anodic photocurrent becomes dominant representing n-type photoconductivity.

The existence of such a critical state has been reported for MnPS$_3$ in an electrolyte with pH of 11.[5] Unfortunately, such harsh electrolyte conditions are not conducive for device fabrication. Recently Wang *et al.* reported the effect of the H$_2$O$_2$ hole scavenger on the photocurrent density of BiFeO$_3$ that also changes the onset of photocurrent.[26] Therefore, the effect of externally added neutral species on the switching potential without changing the pH of electrolyte is important to explore. To study this effect, an inert electrolyte, NaNO$_3$, was added to the electrolytic solution as it is known not to participate in electrochemical or photo-electrochemical charge transfer within the operational potential range because of a relatively negative reduction potential for the NO^{3-}/NO^{2-} couple ($E^o = 0.42$ V vs. RHE) compared to water ($E^o = 1.23$ V vs. RHE) for the O$_2$/H$_2$O couple.[41,42] It is worth mentioning that the addition of NaNO$_3$ to Na$_2$SO$_4$ electrolyte induces only a slight change in pH (from 7.16 to 7.01), which has been duly considered in the
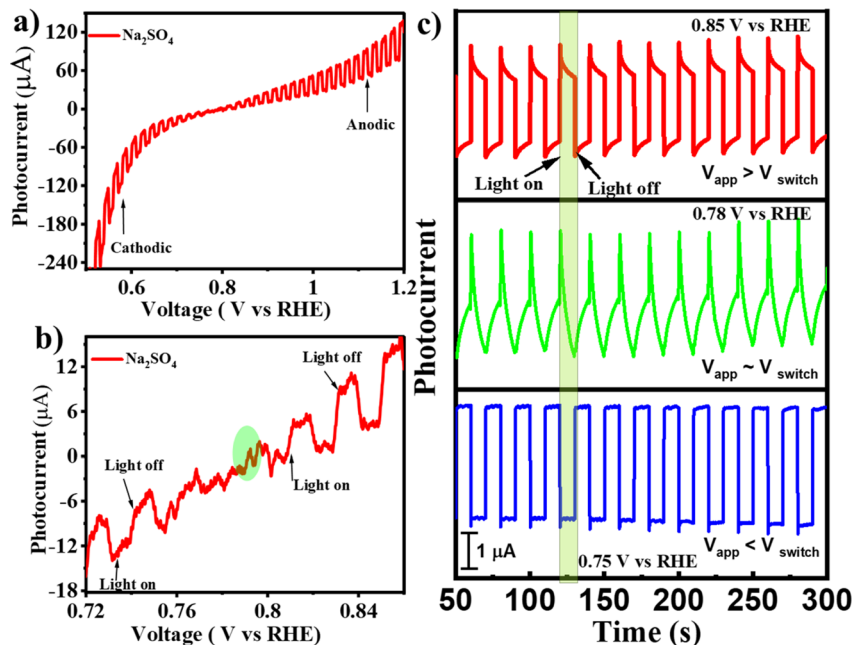
Fig. 3 (a) Photocurrent *vs.* voltage curves for the BFO photoelectrode in Na_2SO_4, (b) enlarged portion showing the switching potential, and (c) transient photocurrent at switching potential and the potential above or below the switching potential.

conversion of the potential scale *vs.* RHE. However, the addition of $NaNO_3$ leads to the excessive presence of NO_3^- ions at the electrode/electrolyte interface that becomes the dominant factor influencing the energetics of the semiconductor/electrolyte interface. The Fermi level of the electrolyte establishes a Nernstian equilibrium with the O_2/OH^- redox couple, and the Nernst equation (eqn (1)) defines the apparent Fermi level, E_F^0.

$$E_F^0 = E_{O_2/OH^-}^0 + \frac{RT}{nF} \ln \left(\frac{O_2}{OH^-} \right) \qquad (1)$$

This change in E_F^0 due to interference of NO_3^- ions would alter the charge transfer dynamics at the interface that might change the switching potential. To verify the hypothesis, photocurrent measurements were performed under simulated solar light (AM 1.5) with intermittent chopping. Fig. 4(a) illustrates photocurrent against V_{app} plots measured for the BFO electrode in Na_2SO_4 with and without addition of $NaNO_3$. Upon increasing the $NaNO_3$ concentration the switching potential shifts anodically from 0.8 V RHE (in 0.1 M Na_2SO_4) to ~0.9 V RHE (in 0.1 M Na_2SO_4 + 0.4 M $NaNO_3$). An enlarged portion of the plot [Fig. 4(b)] clearly illustrates this switch from photocathodic to photoanodic polarity as well as anodic shift in the switching potential. A distinct critical state manifests at the switching potential in all these systems, as depicted in Fig. S5,† which is further verified by chronoamperometry at that potential under chopping of light. To verify that the hypothesis holds true for similar types of anions, we repeated the photocurrent *vs.* voltage measurements by replacing NO_3^- anions with ClO_4^-, keeping the cation fixed (*i.e.*, $NaClO_4$ was used in place of $NaNO_3$). A varying concentration of $NaClO_4$ was added in the Na_2SO_4 electrolyte. Consistent with our initial findings, the anodic shift

in switching potential from 0.8 V RHE (in 0.1 M Na_2SO_4) to ~0.86 V RHE (in 0.1 M Na_2SO_4 + 0.4 M $NaClO_4$) as shown in Fig. S6† was observed. This further supports the impact of specific anion interactions at the semiconductor–electrolyte interface, as predicted using eqn (1). To further verify the validity of eqn (1) in predicting the change in the Fermi level, we conducted a chopped LSV experiment in 0.1 M Na_2SO_4 under two different conditions: (i) in the absence of O_2 and (ii) in O_2-saturated (O_2 was purged for 60 minutes in 20 mL of Na_2SO_4) electrolyte solution. As depicted in Fig. S7,† the switching potential shifted anodically from 0.78 V *vs.* RHE in Na_2SO_4 without O_2 saturation to 0.88 V *vs.* RHE in O_2-saturated solution as per eqn (1).

To understand the origin of the PEPS effect and to explore the impact of variation in electrolyte composition on the electrochemical properties, Mott–Schottky (M–S) analysis was done across all compositions and under O_2 saturated conditions utilizing a three-electrode configuration in a potential range of −1.0 to +1.0 V *vs.* the $Ag/AgCl/Cl^-$ reference electrode at an applied frequency of 1 kHz. As depicted in Fig. 4(c) and S8,† the M–S plot of BFO exhibited a positive slope, indicative of an n-type semiconducting nature, without the formation of any heterojunction with the substrate. Electrochemical impedance spectroscopy (EIS) studies were also performed within a frequency range of 1000 kHz to 100 mHz. Moreover, the flat-band potential (V_{FB}) can be derived from the intercept of the linear portion of M–S curves at the *X*-axis, as determined using eqn (2).[42]

$$\frac{1}{C^2} = \frac{2}{q \, A^2 \, \varepsilon \varepsilon_0 N_D} \left(V - V_{FB} - \frac{k_B T}{q} \right) \qquad (2)$$
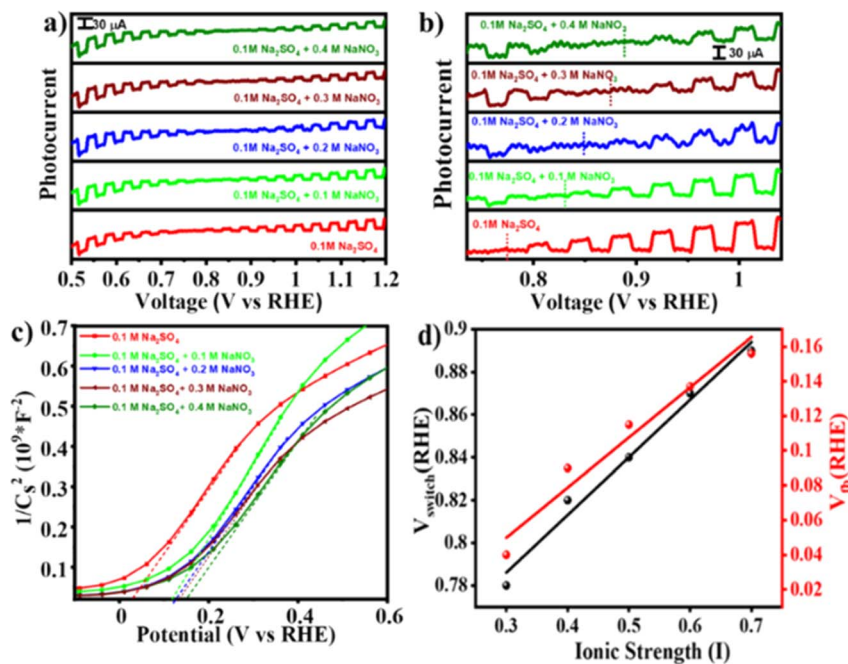
Fig. 4 (a) Photocurrent *vs.* voltage curves for the BFO photoelectrode in different electrolyte compositions, and (b) enlarged portion of (a) showing the switching potential and shift in the onset of photocurrent. Plots of (c) Mott–Schottky, and (d) switching potential *vs.* ionic strength.

Here, C is specific capacitance (F cm^{-2}), q is elementary charge (1.6×10^{-19} C), A is the semiconductor/electrolyte contact area (cm^2), $\varepsilon = 80$ is the relative permittivity of BFO,[43] ε_0 is vacuum permittivity (8.854×10^{-12} F m^{-1}), N_D is donor density (cm^{-3}), V is applied potential (volts), k_B is the Boltzmann constant (1.38×10^{-23} J K^{-1}), and T is the absolute temperature (K).

The V_{FB} obtained using eqn (2) was measured to be 0.03 V *vs.* RHE and consistently exhibited an anodic shift in a trend similar to that of the switching potential when both the inert electrolyte was added and when electrolyte was saturated with O$_2$. On the absolute potential scale, V_{FB} lies between the conduction band edge and the valence band edge of a non-degenerate semiconductor under the flat band conditions. While V_{FB} is typically considered the onset potential of photocurrent, the onset potential tends to be slightly higher than V_{FB} due to slow interfacial charge transfer kinetics necessitating a slight overpotential.[44] With an increase in the concentration of inert electrolyte, both the flat-band potential and the onset of photocurrent shift anodically. Fig. S9† illustrates EIS spectra obtained at OCP (open circuit potential) aimed at assessing the impact of inert electrolyte addition on electrolyte conductivity. The spectra reveal a decrease in solution resistance and a simultaneous increase in ionic conductivity because of inert electrolyte addition.

2.2 PEPS effect and shift in switching potential

Elucidating the precise mechanisms underlying charge transfer proves challenging due to the complex interplay between redox couples in the electrolyte and the solvent. The anodic shift in the photocurrent polarity reversal potential can be explained with the support of the quasi-Fermi level method, band bending

and traditional chemical reaction kinetics to describe the various charge transfer pathways. In a photodetector based on BFO, the O$_2$/OH$^-$ redox couple plays a pivotal role as per eqn (1). In a solution containing 0.1 M Na$_2$SO$_4$, during and after the onset of photocurrent (approximately at 0.8 V *vs.* RHE) a positive trend in photocurrent (I_{ph}) is favoured. Consequently, the positive trend in I_{ph} outweighs the negative trend, resulting in an apparent positive signal in I_{ph}.[5] From eqn (1), it can be predicted that changing the O$_2$/OH$^-$ concentration at the interface would change the Fermi level of the electrolyte. The subsequent additions of NaNO$_3$ and NaClO$_4$ result in an excessive presence of NO$_3^-$ and ClO$_4^-$ ions, relatively lowering the OH$^-$ concentration at the semiconductor–electrolyte interface that changes the Fermi level of the electrolyte system to a more positive value.

This upward shift in the Fermi level of the electrolyte would alter the charge transfer dynamics at the interface as it reduces the width of the space charge layer (W) according to eqn (3) for establishing thermodynamic equilibrium at the interface (Fig. 5). Consequently, the degree of band bending decreases following NaNO$_3$ and NaClO$_4$ addition, and with this, lowering in W continues as more salt is introduced. This argument is supported by the observation of an anodic shift in the flat band potential in M–S plots after NaNO$_3$ addition, indicating a decrease in the width of space charge layer, W, calculated at 0.78 V *vs.* RHE according to eqn (3) and as demonstrated in Fig. S10†.[45]

$$W = \left(\frac{2\varepsilon\varepsilon_0}{qN_D} (V - V_{FB}) \right)^{1/2} \qquad (3)$$
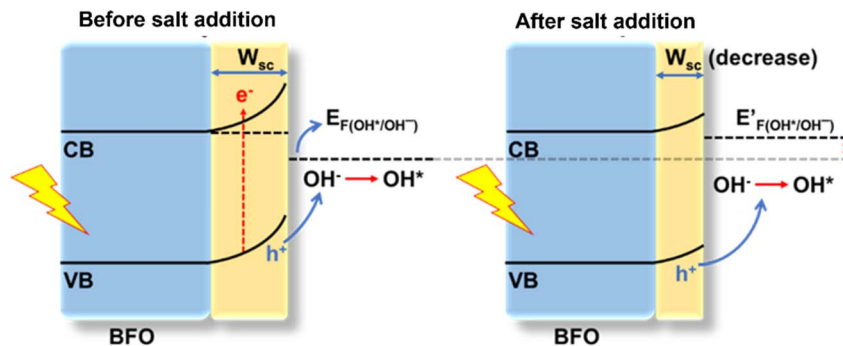
Fig. 5 Mechanism diagram of carrier transport between BFO working electrodes with electrolytes.

Furthermore, a compact double layer at the interface impedes the mobility of OH^- and OH radicals, necessitating a higher overpotential for the completion of reaction pathways. As a result, there is an anodic increase in the photocurrent onset. The composition and concentration of electrolytes along with their respective redox couple concentrations and carrier pathways play a critical role in this process. Thus, a change in the types and concentrations of electrolytes has a significant impact on both the magnitude and polarity of the apparent photocurrent (I_{ph}). Additionally, by altering the electrolytes, the polarity of the output signal from PEC-type photodetectors at a specific potential can be reversed as shown in eqn (4) and (5).

$$OH^- \xrightarrow{k_{et}^{-1}} e^- + OH^· \tag{4}$$

$$h^+ + OH^- \xrightarrow{k_{ht}} OH^· \tag{5}$$

Similarly, increasing the concentration of O_2, an electron acceptor molecule, in Na_2SO_4 solution alters the E_F^0, shifting it to a more positive value. This shift slows the tendency of hydroxyl oxidation, which reduces the space charge layer width and impacts the charge transfer dynamics at the semiconductor–electrolyte interface. As a result, this shift in the E_F^0 leads to an anodic shift in the photocurrent switching potential and an increase in the photocurrent in the cathodic region. The observed changes are further supported by Mott–Schottky plots showing an anodic shift in flatband potential, analogous to the $NaNO_3$ and $NaClO_4$ cases. In PEC systems, not only the concentration of electrons and holes in semiconductors but also the species and concentration of redox couples in electrolytes regulate carrier pathways and trigger the PEPS effect.

3 Conclusion

In summary, a novel, cost-effective, and scalable approach has been shown to synthesize BFO NPs that exhibit a 1.9 eV bandgap, suitable for photoelectrochemical devices. BFO photoelectrodes have been shown to exhibit reversible photocurrent behaviour, which is explained by their distinct bandgap structure, paving the way for the formation of either cathodic or anodic photocurrents based on applied bias. The effect of inert electrolyte on photocurrent switching potential has been investigated in detail and it was found that electrolyte composition may be precisely tailored to provide accurate tuning of photocurrent polarity switching, hence opening a new avenue in the field of photoconversion applications. This study has ramifications not just for BFO but also for other metal oxide perovskites, which might lead to the development of promising switchable photoelectrode materials in the future, especially for compensated semiconductors.

Data availability

All underlying data are available in the published article itself and its ESI.†

Author contributions

Ajay: performed all the experiments, conceptualization, data curation and analysis, and writing of the original draft of the manuscript. JS: data analysis, photo-electrochemical measurements, writing – review and editing. PPI: conceptualization, methodology, writing – review & editing, supervision, and funding acquisition.

Conflicts of interest

The authors declare no competing financial interest.

Acknowledgements

References

1 K. Sivula, R. Zboril, F. L. Formal, R. Robert, A. Weidenkaff, J. Tucek, J. Frydrych and M. Grätzel, *J. Am. Chem. Soc.*, 2010, **132**(21), 7436–7444.

2 L. Meng, Y. Li, R. Yang, X. Zhang, C. Du and J. Chen, *Chem. Commun.*, 2019, **55**, 2182–2185.

3 D. K. Neethipathi, H. S. Ryu, M. S. Jang, S. Yoon, K. M. Sim, H. Y. Woo and D. S. Chung, *ACS Appl. Mater. Interfaces*, 2019, **11**(23), 21211–21217.

4 C. Fan, J. Lai, Z. Shao, X. Zhou, Y. Liu, Y. Lin, L. Ding and K. Wang, *Anal. Chem.*, 2023, **95**(40), 15049–15056.

5 X. Geng, Y. Cai, M. Gao, X. Ma, L. Yu, Y. Xu, W. Shan and M. Qiu, *ACS Appl. Mater. Interfaces*, 2023, **15**(48), 55938–55947.

6 A. Efrati, O. Yehezkeli, R. Tel-Vered, D. Michaeli, R. Nechushtai and I. Willner, *ACS Nano*, 2012, **6**(10), 9258–9266.

7 M. Warzecha, M. Warzecha, M. Oszajca, M. Oszajca, K. Pilarczyk, K. Pilarczyk, K. Szaciłowski and K. Szaciłowski, *Chem. Commun.*, 2015, **51**, 3559–3561.

8 B. Seger, J. McCray, A. Mukherji, X. Zong, Z. Xing and L. Wang, *Angew. Chem., Int. Ed.*, 2013, **52**, 6400–6403.

9 D. K. Singh, P. Prajapat, J. Saroha, R. K. Pant, S. N. Sharma, K. K. Nanda, S. B. Krupanidhi and G. Gupta, *ACS Appl. Electron. Mater.*, 2023, **5**(3), 1394–1400.

10 A. Yucknovsky, Y. Shlosberg, N. Adir and N. Amdursky, *Angew. Chem., Int. Ed.*, 2023, **62**, e202301541.

11 A. Podborska, M. Suchecki, K. Mech, M. Marzec, K. Pilarczyk and K. Szaciłowski, *Nat. Commun.*, 2020, **11**, 854.

12 R. Beranek and H. Kisch, *Angew. Chem., Int. Ed.*, 2008, **47**, 1320–1322.

13 W. S. Bourée, M. S. Prévot, X. A. Jeanbourquin, N. Guijarro, M. Johnson, F. L. Formal and K. Sivula, *Adv. Mater.*, 2016, **28**, 9440.

14 H. Chen, G. Liu, L. Wang, H. Chen, G. Liu and L. Wang, *Sci. Rep.*, 2015, **5**, 12368.

15 C. V. Hoang, K. Hayashi, Y. Ito, N. Gorai, G. Allison, X. Shi, Q. Sun, Z. Cheng, K. Ueno, K. Goda and H. Misawa, *Nat. Commun.*, 2017, **8**, 771.

16 Y. Nishikata, A. Morikawa, M.-A. Kakimoto, Y. Imai, Y. Hirata, K. Nishiyama and M. Fujihira, *J. Chem. Soc., Chem. Commun.*, 1989, 1772–1774.

17 S. Wojtyła and T. Baran, *J. Inorg. Organomet. Polym. Mater.*, 2017, **27**, 436–445.

18 J. Puerres, S. Polanía, A. F. Pérez-Torres, E. A. Erazo, M. T. Cortés and P. Ortiz, *ACS Appl. Nano Mater.*, 2023, **6**(15), 14029–14039.

19 L. Yan, W. Zhao and Z. Liu, *Dalton Trans.*, 2016, **45**, 11346–11352.

20 I. Cesar, K. Sivula, A. Kay, R. Zboril and M. Grätzel, *J. Phys. Chem. C*, 2009, **113**, 772–782.

21 A. Kumar, P. G. Santangelo and N. S. Lewis, *J. Phys. Chem.*, 2002, **96**(2), 834–842.

22 B. Seger, J. McCray, A. Mukherji, X. Zong, Z. Xing and L. Wang, *Angew. Chem., Int. Ed.*, 2013, **52**, 6400–6403.

23 T. Zhao, H. He, C. Wu, L. Lai, Y. Ma, H. Yang, H. Hu, A. Liu, D. Guo and S. Wang, *ACS Appl. Nano Mater.*, 2023, **6**(5), 3856–3862.

24 M. P. Dare-Edwards, J. B. Goodenough, A. Hamnett and P. R. Trevellick, *J. Chem. Soc., Faraday Trans. 1*, 1983, **79**, 2027–2041.

25 P. Salvador, *J. Phys. Chem.*, 2002, **89**, 3764–3773.

26 Y. Wang, M. Daboczi, M. Zhang, J. Briscoe, J.-S. Kim, H. Yan and S. Dunn, *Mater. Horiz.*, 2023, **10**, 5892–5897.

27 J. Ye, S. Jin, Y. Cheng, H. Xu, C. Wu, F. Wu and D. Guo, *ACS Appl. Mater. Interfaces*, 2024, **16**(20), 26512–26520.

28 H. Xu, L. Deng, Y. Cheng, C. Wu, K. Chen and D. Guo, *ACS Appl. Nano Mater.*, 2024, **7**(2), 2359–2369.

29 Y. Cheng, J. Ye, L. Lai, S. Fang and D. Guo, *Adv. Electron. Mater.*, 2023, **9**, 2201216.

30 P. Banoth, C. Kandula, P. K. Lavudya, S. Akaram, L. D. L. S. Valladares, R. Ammanabrolu, G. K. Mamidipudi and P. Kollu, *ACS Omega*, 2023, **8**(21), 18653–18662.

31 S. Yang, G. Ma, L. Xu, C. Deng and X. Wang, *RSC Adv.*, 2019, **9**, 29238–29245.

32 T.-J. Park, G. C. Papaefthymiou, A. J. Viescas, a. A. R. Moodenbaugh and S. S. Wong, *Nano Lett.*, 2007, **7**(3), 766–772.

33 J. Qi, N. Ma, X. Ma, R. Adelung and Y. Yang, *ACS Appl. Mater. Interfaces*, 2018, **10**(16), 13712–13719.

34 D. Tomar and P. Jeevanandam, *J. Magn. Magn. Mater.*, 2022, **564**, 170092.

35 Ajay, V. Tanwar, A. A. Gujare and P. P. Ingole, *Adv. Sustainable Syst.*, 2024, 2400244.

36 X. Shi, S. Quan, L. Yang, C. Liu and F. Shi, *J. Mater. Sci.*, 2019, **54**, 12424–12436.

37 K. P. Remya, D. Prabhu, R. J. Joseyphus, A. C. Bose, C. Viswanathan and N. Ponpandian, *Mater. Des.*, 2020, **192**, 108694.

38 A. H. Ibrahim, Y. M. Abbas, M. H. Ali, H. A. Ayoub and M. Aldoori, *J. Mater. Sci.: Mater. Electron.*, 2024, **35**, 676.

39 N. P. Prasad, M. Rohnke, M. A. Verheijen, J. M. Sturm, J. P. Hofmann, E. J. M. Hensen and A. Bieberle-Hütter, *ACS Appl. Energy Mater.*, 2023, **6**(24), 12237–12248.

40 S. J. Clark and J. Robertson, *Appl. Phys. Lett.*, 2007, **90**, 132903.

41 K.-C. Pan, C.-S. Chuang, S.-H. Cheng and Y. O. Su, *J. Electroanal. Chem.*, 2001, **501**, 160–165.

42 K. Sivula, *ACS Energy Lett.*, 2021, **6**(7), 2549–2551.

43 J. Lu, A. Günther, F. Schrettle, F. Mayr, S. Krohns, P. Lunkenheimer, A. Pimenov, V. D. Travkin, A. A. Mukhin and A. Loidl, *Eur. Phys. J. B*, 2010, **75**, 451–460.

44 A. Hankin, F. E. Bedoya-Lora, J. C. Alexander, A. Regoutz and G. H. Kelsall, *J. Mater. Chem. A*, 2019, **7**, 26162–26176.

45 K. K. Dey, S. Gahlawat and P. P. Ingole, *J. Mater. Chem. A*, 2019, **7**, 21207–21221.